



# Mechanochemical preparation of ceria-zirconia catalysts for the total oxidation of propane and naphthalene Volatile Organic Compounds

Parag M. Shah, Andrew N. Day, Thomas E. Davies, David J. Morgan, Stuart H. Taylor\*

*Cardiff Catalysis Institute, School of Chemistry, Cardiff University, Main Building, Park Place, Cardiff, CF10 3AT, UK*



## ARTICLE INFO

### Keywords:

Ceria  
Zirconia  
VOCs  
Mechanochemical preparation  
Propane  
Naphthalene

## ABSTRACT

A range of ceria-zirconia mixed metal oxide catalysts were synthesised by mechanochemical milling from nitrate precursors and tested for propane and naphthalene total oxidation. The mixed CeZrO<sub>x</sub> metal oxide catalysts were more active compared to pure CeO<sub>2</sub> and ZrO<sub>2</sub>, with the Ce<sub>0.90</sub>Zr<sub>0.10</sub>O<sub>x</sub> catalyst the most active for both propane and naphthalene total oxidation. Catalysts were characterised by XRD, TGA, Raman spectroscopy, BET surface area, XPS, TEM and SEM-EDX techniques. Formation of CeZrO<sub>x</sub> solid solutions were observed for Zr content ranging from 5 to 25%, and phase separated materials were observed for higher Zr content of 50%. The incorporation of Zr into the CeO<sub>2</sub> lattice increased the surface area compared to pure CeO<sub>2</sub> and ZrO<sub>2</sub>, with evidence of a surface enrichment of Zr when concentrations were compared to the bulk. Incorporation of Zr was found to increase the surface concentration of oxygen defects in the CeZrO<sub>x</sub> mixed metal oxides, the concentration of these defect on the catalysts follows a similar trend to the propane and naphthalene total oxidation activity. The increased presence of oxygen defects and reducibility are factors responsible for the enhanced total oxidation activity of the mixed metal oxide catalysts and the mechanochemical method is an effective preparation route for these active catalysts.

## 1. Introduction

Short chain and aromatic hydrocarbons form part of the wider range of atmospheric organic pollutants called Volatile Organic Compounds (VOCs). Short chain alkanes are amongst some of the most stable VOCs and can persist in the lower and upper atmosphere for a considerable time [1]. VOCs are generally potent greenhouse gases, and are responsible for atmospheric radical processes which lead to the formation of ground level ozone [2,3]. VOC species can react with NO to produce NO<sub>2</sub> [4], or agglomerate and condense to form soot and particulate matter [5,6]. Hence, there is a need to reduce harmful emissions of VOCs.

The move away from traditional fossil fuels such as petrol and diesel for transportation has led to a significant increase in the use of liquefied propane gas (LPG), which is a mixture of propane and butane. Over 2.4 million barrels of LPG were consumed in the US each day in 2012 [7], with this number increasing year on year, and becoming > 4 million barrels in 2014. LPG provides a cleaner combustion compared to conventional fuels [8], however, the use of LPG is contributing to increased levels of atmospheric propane emissions [9]. Propane, and other short chain alkanes, are also emitted from a range of stationary processing and manufacturing sources. Another common compound emitted

during the combustion of diesel and other organic materials is naphthalene [10]. Naphthalene is the simplest member of the poly-aromatic hydrocarbon family of compounds, which can cause a wide range of harmful effects and are known carcinogens, so it is essential that release to the atmosphere is abated.

A number of technologies can be employed to control emission of VOCs, these include thermal oxidation, catalytic oxidation, adsorption and absorption. Catalytic oxidation is recognised as one of the most efficient and flexible, as it provides the potential to destroy pollutants totally to carbon dioxide and water, removing them to low levels, and has the ability to treat effluent containing a range of VOC concentrations [11]. VOCs are wide ranging in chemical functionality and their emission sources, but it is clear that linear short chain alkanes, which we target in this work, are some of the most difficult to destroy by catalytic oxidation [1]. Effective VOC oxidation catalysts have to deal with a wide range of VOCs and so it is interesting to compare activity for different organic compounds. Accordingly, in this study we have investigated the catalytic oxidation of propane and naphthalene.

Supported noble metal catalysts make up around 75% of VOC total oxidation catalysts [12], and now there is a desire to move towards cheaper and more abundant metal oxide catalysts. CeO<sub>2</sub> is a widely studied metal oxide catalyst due to its favourable redox properties and

\* Corresponding author.

E-mail address: [taylorsh@cardiff.ac.uk](mailto:taylorsh@cardiff.ac.uk) (S.H. Taylor).

ability to form non-stoichiometric  $\text{CeO}_{2-x}$ , leading to oxygen vacancies and active surface  $\text{O}_2$  species [13–15].  $\text{ZrO}_2$  can also form oxygen vacancies due to paramagnetic F-centres which can excite and activate surface  $\text{O}_2$  [16]. When  $\text{ZrO}_2$  is combined with  $\text{CeO}_2$  the mobility of lattice oxygen species and oxygen storage capacity are increased, due to an increase of reducibility of  $\text{Ce}^{4+}$  to  $\text{Ce}^{3+}$  and its ability to diffuse both surface and bulk oxygen [17–19]. Additionally, the thermal resistance of the mixed metal oxides, compared to the single metal oxide counterparts, are enhanced, leading to increased stability when used for high temperature VOC oxidation [18].

Ceria-zirconia mixed metal oxide catalysts have been tested for oxidation of a range of VOCs, including naphthalene [20,21], and other environmental pollutants, such as methane [22] and diesel soot particulates [23]. However, there is very limited literature on the total oxidation of propane using  $\text{CeZrO}_x$  catalysts. Pt and Pd nanoparticles supported on Ceria-Zirconia catalysts have been synthesised and reported to be active for propane total oxidation [24,25]. These studies reported that mixed Ce-Zr metal oxide catalysts were more active than pure  $\text{CeO}_2$  and  $\text{ZrO}_2$ , with incorporation of low concentrations of Zr noted to be the most active.

The method of catalyst manufacture can also have an environmental impact. Preventing waste and using safer chemical synthesis routes are central ideas from the 12 Principles of Green Chemistry [26]. The principles are often applied to synthetic chemical procedures, but they apply equally to processes like catalyst preparation. Mechanochemical synthesis is one such catalyst preparation route that can be considered green and has a number of advantages when compared to other more conventional routes [27]. Conventional methods of mixed metal oxide preparation such as sol-gel and co-precipitation produce waste solvents requiring energy intensive means of purification of the by-product downstream. Mechanochemical preparation also has the advantage of reducing the concentration of surface poisons, such as  $\text{Na}^+$  or  $\text{K}^+$ , introduced from basic precipitating agents, leading to potentially more active catalysts [28]. Many mechanochemically prepared catalysts such as tin doped ceria-zirconia combined with  $\text{Pd}/\text{Al}_2\text{O}_3$  [29], and vanadium-diphosphate [30], have also been reported to have higher surface area and oxygen storage capacity compared to other preparation methods.  $\text{CeO}_2\text{-ZrO}_2$  solid solutions have been prepared previously by mechanical mixing of the oxides [31–33] but to date the preparation of active catalyst by direct milling of the nitrates has not been reported.

The aim of this study is to prepare an active and stable ceria-zirconia mixed metal oxide catalyst for the total oxidation of propane and naphthalene, investigating mechanochemical grinding as a potential method for catalyst synthesis. The aim is to study the influence of zirconia content on ceria, characterising the surface and structure, and relating these features to catalyst performance for total propane and naphthalene oxidation.

## 2. Experimental

### 2.1. Catalyst preparation

A range of ceria-zirconia mixed metal oxide catalysts were prepared using a Retsch PM100 planetary orbital ball mill in a 10 cm  $\text{ZrO}_2$  lined crucible containing seven 15 mm  $\text{ZrO}_2$  balls.  $\text{Ce}(\text{NO}_3)_3 \cdot 6\text{H}_2\text{O}$  (Sigma-Aldrich, 99%) and  $\text{ZrO}(\text{NO}_3)_2 \cdot x\text{H}_2\text{O}$  (Sigma-Aldrich, 99%) were used as starting materials. The Ce:Zr molar ratios investigated were 100:0, 95:5, 90:10, 75:25, 50:50 and 0:100. The metal nitrates were lightly ground together before being placed into the crucible. The mixtures were then ground in the ball mill at 300 rpm for 4 h at room temperature. The powders were collected and calcined under flowing air (400 °C for 3 h, with a ramp rate of 1 °C min<sup>-1</sup> from ambient).

### 2.2. Catalyst characterisation

Thermal gravimetric analysis (TGA) of the post ball-milled samples

was undertaken to assess the thermal stability of the catalyst precursors. Approximately 50 mg of sample was placed into a Perkin Elmer TGA 4000 instrument and heated from 30 to 500 °C at a rate of 5 °C min<sup>-1</sup> under a flowing  $\text{N}_2$  atmosphere.

Catalysts surface areas were determined using a Quantachrome Quadrasorb Evo analyser. Catalyst samples were degassed under vacuum at 250 °C for 16 h. The surface area was determined from collection of 5-point  $\text{N}_2$  adsorption isotherms measured at –196 °C and data treated using the BET method.

Powder X-ray diffraction (XRD) patterns were collected using a Panalytical X'Pert diffractometer with a Cu X-ray source operating at 40 kV and 40 mA. Phase identification was performed by matching experimental patterns against entries in the ICDD standard database. Crystallite size was estimated by X-ray line broadening using the Scherrer equation by comparing experimental line widths against a highly crystalline Si standard. The (200) diffraction peak was used to calculate the lattice parameters and unit cell volume. These were calculated from data collected using a sample with contained 10% Si as an internal standard.

*In situ* XRD analysis was also carried out on the uncalcined  $\text{Ce}_{0.50}\text{Zr}_{0.50}\text{O}_x$  sample using a Panalytical X'Pert diffractometer with an Anton Paar 900 K *in situ* cell. Data were collected by heating the sample from 200 to 600 °C under a flow of air (30 ml min<sup>-1</sup>), holding the temperature isothermally at 50 °C intervals for 30 min to acquire data.

Raman spectra were obtained using a Renishaw inVia confocal Raman microscope equipped with an  $\text{Ar}^+$  visible green laser with an emission of wavelength of 514 nm. The catalyst samples were placed onto a steel plate and spectra were collected in a reflective mode by a highly sensitive charge couple device (CCD) detector.

X-ray photoelectron spectroscopy (XPS) was carried out using a Thermo Scientific K-Alpha<sup>+</sup> Spectrometer, equipped with an Ar ion source and Al  $K\alpha$  micro-focused monochromator operating at 72 W (6 mA, 12 kV). Survey and high resolution scans were carried out at pass energies of 150 and 40 eV respectively with a 1 or 0.1 eV step size. Charge neutralisation was achieved using a combination of flux of low-energy electrons and Ar ions. Spectra were calibrated against the C(1 s) peak at 284.8 eV. XPS data were analysed using CasaXPS (v2.3.19rev1.1 l), using Scofield sensitivity factors and an energy dependence of -0.6, after removal of a Shirley background.

Microscopy was performed on a Tescan MAIA3 field emission gun scanning electron microscope (FEG-SEM) fitted with secondary and backscattered electron detection. Energy-dispersive X-ray (EDX) analysis and mapping was performed using an Oxford Instruments X-Max<sup>N</sup> 80 detector and the data analysed using the Aztec software. EDX analysis was performed using the Oxford Aztec Point and ID software. A minimum of 5 areas were analysed across multiple particles and averaged. Transmission electron microscopy (TEM) was performed on a Jeol JEM 2100 LaB<sub>6</sub> microscope operating at 200 kV. Samples were dry mounted on 300 mesh copper grids coated with holey carbon film.

Temperature Programmed Reduction (TPR) was performed using a Quantachrome ChemBET TPD/R/O apparatus. Samples were pretreated under a flow of He at 120 °C for 1 h prior to analysis. Reduction profiles were obtained by analysing *ca.* 30 mg of catalyst under a flow of 10%  $\text{H}_2$  in Ar (30 ml min<sup>-1</sup>) over a temperature range from ambient to 1100 °C with a ramp rate of 15 °C min<sup>-1</sup>.

### 2.3. Catalyst testing

Catalyst performance for propane total oxidation was measured using a continuous flow fixed bed microreactor. Catalysts samples were placed into a 6 mm o.d. stainless steel tube and secured between two plugs of quartz wool. A premixed cylinder of 5000 vppm propane in synthetic air was used (BOC Speciality Gases) with the gas flow regulated by electronic mass flow controllers (50 ml min<sup>-1</sup>). The catalyst powders were packed un-pelleted to a constant volume (0.06 mL, *c.a.* 0.44 g) to achieve a gas hourly space velocity (GHSV) of 45,000 h<sup>-1</sup>.

The activity was measured over a temperature range of 200–600 °C, with the temperature maintained and controlled by a K-type thermocouple placed into the catalyst bed. The catalyst was allowed to stabilise at each temperature before analysing the reactor effluent. The reaction effluent was analysed by an online gas chromatograph (Agilent 7090B) with detectors in series. A thermal conductivity detector, to analyse O<sub>2</sub> and N<sub>2</sub>, and flame ionisation detector equipped with a methaniser, to analyse CO, CO<sub>2</sub> and hydrocarbons were used. Separation was achieved using a Haysep Q (80–100 mesh, 1.8 m x 3.2 mm) and MolSieve 13 X (80–100 mesh, 2 m x 3.2 mm) packed columns, with a series/by-pass valving configuration. Analyses were performed at each temperature until steady-state was attained and three consistent sets of analytical data were obtained. The reaction was then increased to the next temperature, and after appropriate stabilisation time to re-establish steady-state the analysis procedure was repeated.

Naphthalene total oxidation was evaluated using a second continuous flow fixed bed reactor. The catalyst powders were packed un-pelleted to a constant volume (0.06 mL, c.a. 0.44 g) in a 6 mm o.d. stainless steel tube between plugs of quartz wool to provide a GHSV of 45,000 h<sup>-1</sup>. 100 vppm naphthalene was generated by subliming naphthalene in a thermostatically controlled heater at 35 °C under a He flow (40 ml min<sup>-1</sup>). O<sub>2</sub> (10 ml min<sup>-1</sup>) was then added to provide a total flow of 50 ml min<sup>-1</sup>. The gas flow was then passed through the reactor tube containing the catalyst, which was heated in a clam-shell furnace. The activity was measured over a temperature range of 100–250 °C at 25 °C intervals, with the temperature monitored using a k-type thermocouple placed in the catalyst bed. The reaction effluent was analysed using an Agilent 7090B GC (columns: HP-5, 30 m x 0.32 mm x 0.25 µm and Haysep Q, 80–100 mesh, 3 m x 3.2 mm), with a methaniser and 2 FID detectors. Four analyses were undertaken at each temperature after 1 h of stabilisation. The reaction temperature was then increased to the next value, and after appropriate stabilisation time to attain steady-state the analysis procedure was repeated.

### 3. Results and discussion

#### 3.1. Catalyst precursor characterisation

Thermal gravimetric analysis profiles for the decomposition of the milled (ZrO(NO<sub>3</sub>)<sub>2</sub>.xH<sub>2</sub>O and Ce(NO<sub>3</sub>)<sub>3</sub>.6H<sub>2</sub>O) prior to calcination are shown in Fig. 1. Both profiles showed three weight loss events. The first major loss from 100 to 150 °C is from desorption of physisorbed H<sub>2</sub>O, contributing a total loss of 30% and 15% for the milled Zr and Ce nitrate precursors respectively. The second weight loss takes place from 250 to 350 °C and occurs in two stages. It is attributed to the loss of crystallized water and subsequent decomposition of the nitrate. The decomposition under nitrogen atmosphere is more complex than under air where one would typically see a single weight loss leading to oxide

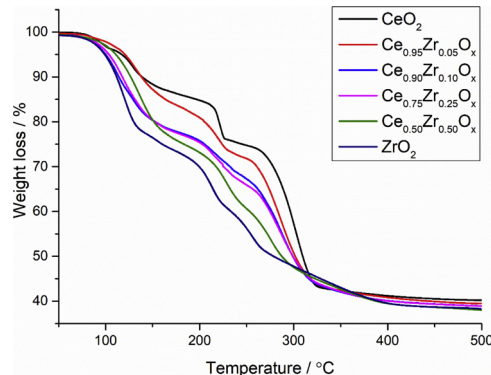


**Fig. 1.** Thermogravimetric analysis of the pre-calcined mechanochemically prepared CeO<sub>2</sub>, ZrO<sub>2</sub> and CeZrO<sub>x</sub> mixed metal oxide catalysts. Samples heated in flowing N<sub>2</sub> atmosphere from 30 to 500 °C at 5 °C min<sup>-1</sup>.

formation. This three stage weight loss has been previously reported in the literature for cerium nitrate and is attributed to the formation of an anhydrous Ce(NO<sub>3</sub>)<sub>3</sub> intermediate [34]. The ZrO(NO<sub>3</sub>)<sub>2</sub>.xH<sub>2</sub>O decomposition onset occurs at 220 °C, whereas the nitrate in Ce(NO<sub>3</sub>)<sub>3</sub>.6H<sub>2</sub>O starts to decompose at 260 °C, which accounts for 30% and 45% weight loss for the Zr and Ce nitrate precursors respectively. The weight losses are very similar to the theoretical value expected for the formation of the metal oxides CeO<sub>2</sub> and ZrO<sub>2</sub>. This suggests very little H<sub>2</sub>O and NO<sub>x</sub> were lost due to the thermal effects of grinding.

Fig. 1 also shows the mass loss profiles of the CeZrO<sub>x</sub> mixed metal oxide catalyst precursors produced mechanochemically. All mixed CeZrO<sub>x</sub> catalyst precursors, regardless of the ratio, showed a reduction in the nitrate decomposition temperature compared to cerium nitrate, whilst they were increased relative to zirconium nitrate. The mixed CeZrO<sub>x</sub> precursors all showed nitrate decomposition between the limits of the single component cerium and zirconium nitrates, rather than showing clear additive traces of the single nitrates. This observation may be interpreted that there is intimate mixing of the cerium and zirconium precursors after milling.

In order to gain some understanding of transformations during calcination of the precursors to form the final catalysts, *in situ* XRD under flowing air was employed. The Ce<sub>0.50</sub>Zr<sub>0.50</sub>O<sub>x</sub> precursor was selected as a representative material for study (Fig. 2). Diffraction patterns of the non-calcined sample indicates the presence of numerous Ce and Zr nitrate and hydroxy phases. The pattern obtained at 200 °C only has Ce, Zr and mixed nitrate precursor phases present, the H<sub>2</sub>O and OH groups are not observed which is consistent with their loss in the TGA profile. As the temperature is increased the intensity of reflections attributed to the precursor species decrease and at 250 °C there is the emergence of a diffraction peak at 28.4°, indicating the formation of (111) lattice planes of the CeO<sub>2</sub> cubic fluorite structure. No diffraction from the (101) lattice planes of tetragonal ZrO<sub>2</sub> (29.9°) was observed at 250 °C; they were only observed when the temperature was increased above 450 °C. The higher temperature caused the Zr to segregate from the CeO<sub>2</sub> phase and the formation of a bulk tetragonal ZrO<sub>2</sub> phase was observed [35–37].

Based on the *in situ* XRD and TGA analysis, a calcination temperature of 400 °C was selected for catalyst preparation, as this resulted in full decomposition of the precursors and formation of mixed oxide phases, whilst minimising cerium and zirconium phase segregation.

#### 3.2. Catalyst performance

Fig. 3 shows the catalytic activity for the total oxidation of propane

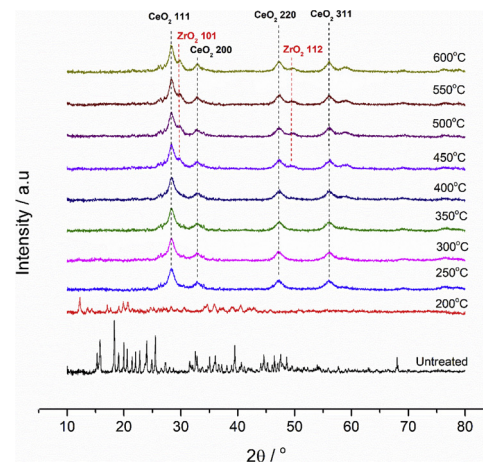


**Fig. 2.** *In situ* powder X-ray diffraction patterns of the Ce<sub>0.50</sub>Zr<sub>0.50</sub>O<sub>x</sub> catalyst precursor showing the formation of the CeO<sub>2</sub> cubic fluorite phase and formation of the tetragonal ZrO<sub>2</sub> phase at 450 °C. Reaction conditions: 200–600 °C under a flow of 30 mL min<sup>-1</sup> air, 10 min scan duration.

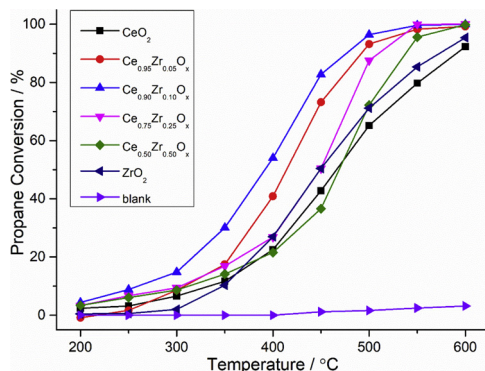
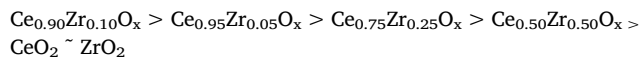
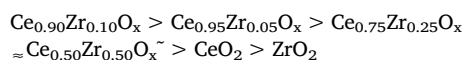


**Fig. 3.** Catalytic activities for the total oxidation of propane over the CeO<sub>2</sub>, ZrO<sub>2</sub> and CeZrO<sub>x</sub> catalysts. Reaction conditions: GHSV = 45,000 h<sup>-1</sup>, Temperature range: 200–600 °C, 5000 vppm propane in air for all experiments. Legend refers to the different Ce:Zr ratios.

for the range of CeZrO<sub>x</sub> mixed metal oxide catalysts prepared using mechanochemical grinding. A blank run with no catalyst showed only 3% propane conversion at 600 °C, indicating that the contribution of homogeneous gas phase reactions was negligible under conditions of catalytic activity. All catalysts showed appreciable propane oxidation activity, and all had very high selectivity to CO<sub>2</sub> (> 99%). Both CeO<sub>2</sub> and ZrO<sub>2</sub> showed similar activity profiles with 100% propane conversion achieved at 600 °C. Upon addition of Zr to cerium oxide there was an increase in the activity compared to the CeO<sub>2</sub> and ZrO<sub>2</sub>. The order of catalyst activity over the range of propane conversion followed the general trend:



The catalytic activity for the CeZrO<sub>x</sub> mixed metal oxide catalysts for the total oxidation of naphthalene is shown in Fig. 4. A blank reaction showed minimal naphthalene oxidation activity over the temperature range of the experiment, again indicating negligible conversion of naphthalene by gas phase oxidation. The CeO<sub>2</sub> and ZrO<sub>2</sub> showed similar low activity profiles, with only 20% CO<sub>2</sub> yield at 250 °C. The CeZrO<sub>x</sub> mixed metal oxide catalysts all showed significant activity with all catalysts producing 100% CO<sub>2</sub> yield at 250 °C. A similar general trend for naphthalene total oxidation activity to that for propane total oxidation was observed, the trend is:



A similar trend was also observed for the total oxidation of

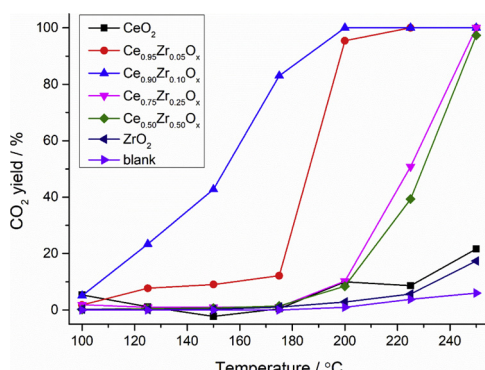


**Fig. 4.** Catalytic activities for the total oxidation of naphthalene over the CeO<sub>2</sub>, ZrO<sub>2</sub> and CeZrO<sub>x</sub> catalysts. Reaction conditions: GHSV = 45,000 h<sup>-1</sup>, Temperature range: 100–250 °C, 100 vppm naphthalene in 20% O<sub>2</sub> balanced with He for all experiments. Legend refers to the different Ce:Zr ratios.

naphthalene using ceria-zirconia mixed metal oxide catalysts prepared by co-precipitation with both urea and sodium carbonate [20]. Previous co-precipitation prepared catalysts also demonstrated that addition of lower Zr concentrations produced catalysts with higher activity for VOC oxidation than the parent CeO<sub>2</sub>.

### 3.3. Catalyst characterisation

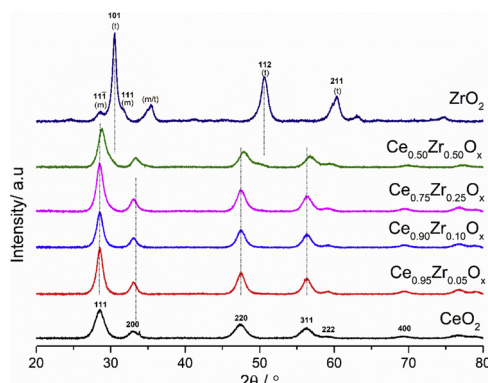
**Table 1** shows a summary of characterisation data for the range of ceria-zirconia catalysts. The mechanochemical prepared catalysts have similar surface areas compared to conventional catalyst synthesis methods [20,35,38,39]. Many studies have reported that there is an increase in surface area upon addition of Zr into the CeO<sub>2</sub> lattice [38,40]. The same effect is observed for the catalysts prepared mechanochemically from the nitrate precursors, as the addition of any amount of Zr led to an increase in the surface area compared to CeO<sub>2</sub>. There was no significant systematic trend of surface area with the variation of Zr content, as all mixed metal oxide catalysts were broadly similar, and were in the range 109–130 m<sup>2</sup> g<sup>-1</sup>, compared to surface areas of ca. 90 m<sup>2</sup> g<sup>-1</sup> for both CeO<sub>2</sub> and ZrO<sub>2</sub>. It should also be noted that the increase in surface area cannot be solely attributed to the effect of Zr incorporation as milling is also expected to result in a decrease in particle size and hence an increase in inter-particle surface area. Comparison to the previously reported surface areas obtained by milling show that in this case the surface areas are significantly larger than those reported by Carbajal-Ramos and Trovelli (ca. 30–50 m<sup>2</sup> g<sup>-1</sup>) [31,33,41] although these were synthesised by a mechano-chemical route using NaCl or direct reaction of the oxides respectively. In this case it is apparent that mechanical processing directly from the nitrates affords catalysts with surface areas twice the size of those currently reported in the literature. The effect of surface area on naphthalene total oxidation using unmodified CeO<sub>2</sub> catalysts has been investigated previously [42], with high surface area being a factor contributing to more active catalysts. **Table 1** shows indicative surface area normalised propane oxidation rates for the single and mixed metal oxide catalysts prepared mechanochemically. The normalised rates showed a range of values, indicating that there was no simple relationship with the increased surface area of the mixed ceria-zirconia catalysts and their increased activity over ceria, hence other factors were also responsible for the enhanced catalyst performance.

Powder XRD patterns of the CeZrO<sub>x</sub> mixed metal oxide catalysts are shown in Fig. 5, and further derived data are presented in Table 2. The CeO<sub>2</sub> is present in the cubic fluorite phase with characteristic reflections around 28.8°, 33.6°, 49.3° and 57.0°, representing diffraction from the (111), (200), (220) and (311) lattice planes respectively [20,43]. The ZrO<sub>2</sub> pattern shows both the monoclinic and tetragonal phase. The major tetragonal reflections are indicated at 30.2°, 34.8°, 50.7° and 59.6°, corresponding to the (101), (110), (112) and (211) lattice planes respectively [44]. Monoclinic ZrO<sub>2</sub> is identified by the small shoulders apparent at 28.8 and 31.6° corresponding to the (11-1) and (111) planes as indicated in the figure. Selected area electron diffraction, (Fig. 6), confirms the presence of the cubic fluorite structure for ceria with diffraction rings indexed to the (111), (200), (220) and (311) planes (Fig. 6a). The patterns are consistent with a polycrystalline material comprising small randomly orientated crystallite domains. The zirconia shows diffraction rings consistent with a mixture of the monoclinic and tetragonal phases (Fig. 6f) [45].

Analysis of the mixed ceria-zirconia catalysts by XRD showed that no diffraction from a discrete ZrO<sub>2</sub> phase was observed for any of the catalysts. All the mixed catalysts showed diffraction attributed to a CeO<sub>2</sub> cubic fluorite phase. However, the intensity of the reflections decreased and broadened as the zirconium concentration increased. With zirconium addition there was a shift in the diffraction angle of the CeO<sub>2</sub> peaks to higher values, Table 2. With no discrete reflections from a ZrO<sub>2</sub> phase, this suggests the CeO<sub>2</sub> bulk cubic fluorite structure remains, indicating the formation of a CeZrO<sub>x</sub> mixed metal oxide solid

**Table 1**Physiochemical properties of the range of  $\text{CeO}_2$ ,  $\text{ZrO}_2$  and  $\text{CeZrO}_x$  mixed oxide catalysts.

Catalyst	BET surface area <sup>a</sup> / $\text{m}^2 \text{ g}^{-1}$	Propane oxidation rate ( $\times 10^{-8}$ ) <sup>b</sup> / $\text{mol s}^{-1} \text{ m}^{-2} \text{ g}^{-1}$	Raman FWHM <sup>c</sup> / $\text{cm}^{-1}$	Normalised composition (Ce:Zr) <sup>d</sup>	Surface reduction <sup>e</sup> / $\mu\text{mol H}_2 \text{ g}^{-1}$	Surface reduction <sup>f</sup> / $\mu\text{mol H}_2 \text{ m}^{-2}$
$\text{CeO}_2$	88	1.68	28.6	100:0	87	0.99
$\text{Ce}_{0.95}\text{Zr}_{0.05}\text{O}_x$	127	2.00	33.3	93.1:6.9	168	1.32
$\text{Ce}_{0.90}\text{Zr}_{0.10}\text{O}_x$	130	2.21	32.5	89.2:11.8	185	1.42
$\text{Ce}_{0.75}\text{Zr}_{0.25}\text{O}_x$	109	1.60	34.5	78.3:21.7	180	1.65
$\text{Ce}_{0.50}\text{Zr}_{0.50}\text{O}_x$	124	1.02	44.9	50.8:49.2	153	1.23
$\text{ZrO}_2$ <sup>f</sup>	93	1.87	—	0:100	—	—

<sup>a</sup> From 5 point  $\text{N}_2$  adsorption.<sup>b</sup> Rate at 450 °C.<sup>c</sup> Data from peak at 464  $\text{cm}^{-1}$ .<sup>d</sup> From EDX measurement.<sup>e</sup> From TPR profile using 30 mg catalyst.<sup>f</sup> Surface reduction measurement not applicable.

**Fig. 5.** Powder X-ray diffraction patterns of the  $\text{CeO}_2$ ,  $\text{ZrO}_2$  and  $\text{CeZrO}_x$  calcined at 400 °C. The  $\text{ZrO}_2$  shows both the tetragonal (t) and monoclinic (m) phases. The formation of the tetragonal  $\text{ZrO}_2$  phase is apparent in the  $\text{Ce}_{0.50}\text{Zr}_{0.50}\text{O}_x$  catalyst.

solution with the cubic fluorite structure [20,46].

The average crystallite size was calculated from the powder XRD patterns using the Scherrer equation by taking an average of the values obtained by analysing the peak widths of the 4 dominant reflections ((111), (200), (220), and (311)). The addition of Zr to the ceria caused a general decrease of the crystallite size, when compared to the ceria alone. The decrease in crystallite size was relatively small, and there was no systematic trend with increasing the concentration of Zr, however, the decrease in crystallite size is consistent with the relatively small increase of surface area that was also observed.

The cubic fluorite unit cell volume was calculated using the d-spacing for the (200) lattice plane and results are shown in Table 2. The  $\text{CeO}_2$  has the highest unit cell volume, with the unit cell volume

decreasing linearly upon increasing the Zr content of the  $\text{CeZrO}_x$  mixed metal oxide. Vegard's Law can be used to determine the extent of the Zr incorporation into the  $\text{CeO}_2$  lattice [47], which is shown in Table 2. All the  $\text{CeZrO}_x$  mixed metal oxide catalysts have some Zr incorporated into the  $\text{CeO}_2$ , however the quantity incorporated is much lower compared to the maximum allowed based on the original preparation ratios. Most samples only have ~20% of the total Zr incorporated into the  $\text{CeO}_2$  lattice. The Zr that is not incorporated into the Ceria lattice is not visible by XRD, indicating it is present as amorphous material or is highly dispersed domains which do not have sufficient diffracting capacity.

Catalysts were also characterised using laser Raman spectroscopy (Fig. 7). Only one Raman active mode is expected for the cubic fluorite  $\text{CeO}_2$  phase ( $F_{2g}$ ) at 464  $\text{cm}^{-1}$  [43]. Six Raman active modes at 131, 247, 307, 464, 596 and 626  $\text{cm}^{-1}$  are expected for a tetragonal  $\text{ZrO}_2$  phase ( $A_{1g} + 3E_g + 2B_{1g}$ ) [48]. From the Raman spectra only one mode is seen for  $\text{CeO}_2$ ,  $\text{Ce}_{0.95}\text{Zr}_{0.05}\text{O}_x$ ,  $\text{Ce}_{0.90}\text{Zr}_{0.10}\text{O}_x$ ,  $\text{Ce}_{0.75}\text{Zr}_{0.25}\text{O}_x$  and  $\text{Ce}_{0.50}\text{Zr}_{0.50}\text{O}_x$ , centred at 464  $\text{cm}^{-1}$ , representing the fluorite  $\text{CeO}_2$  as observed from XRD. The zirconia only catalyst Raman spectrum (Fig. 7b) has been expanded 7.5 times, to more readily display the discrete peaks present; these are centred at 260, 315, 464 and 640  $\text{cm}^{-1}$  and indicate the presence of tetragonal  $\text{ZrO}_2$ , supporting the XRD findings.

With the addition of increasing concentrations of Zr the peak at 464  $\text{cm}^{-1}$  red shifts to higher wavenumbers with the  $\text{Ce}_{0.50}\text{Zr}_{0.50}\text{O}_x$  catalyst having a peak position of 467  $\text{cm}^{-1}$ . This has been determined to be as a result of the decreased order of the system as a consequence of the Ce substitution for Zr. There is also a simultaneous reduction in peak intensity due to the reduced crystallinity and particle size of the cubic  $\text{CeO}_2$  phase (Table 1) which is known to lead to the broadening of the Raman band [49]. Full width half maximum (FWHM) values of the peaks have been calculated from the fluorite  $\text{CeO}_2$  Raman band at

**Table 2**Crystallographic properties of the  $\text{CeO}_2$ ,  $\text{ZrO}_2$  and  $\text{CeZrO}_x$  mixed metal oxide catalysts calculated from powder X-ray diffraction data.

Catalyst	Average crystallite size <sup>a</sup> / $\text{\AA}$	(200) d-Spacing / $\text{\AA}$	Lattice parameter <sup>b</sup> / $\text{\AA}$	Unit cell volume <sup>b</sup> / $\text{\AA}^3$	Incorporation of Zr into ceria <sup>c</sup> / %	Incorporation of Zr into ceria <sup>d</sup> / %
$\text{CeO}_2$	118	2.694	5.388	156.436	—	—
$\text{Ce}_{0.95}\text{Zr}_{0.05}\text{O}_x$	105	2.692	5.383	156.067	1.52	1.52
$\text{Ce}_{0.90}\text{Zr}_{0.10}\text{O}_x$	95	2.691	5.382	155.921	2.14	1.82
$\text{Ce}_{0.75}\text{Zr}_{0.25}\text{O}_x$	103	2.684	5.369	154.749	7.07	5.76
$\text{Ce}_{0.50}\text{Zr}_{0.50}\text{O}_x$	97	2.667	5.334	151.766	19.6	16.36
$\text{ZrO}_2$	99	2.550 [60]	5.100	132.651	—	—

<sup>a</sup> Using Scherrer equation, based on average value from (111), (200), (220) and (311) peaks.<sup>b</sup> Calculated from (200) lattice plane with Si standard.<sup>c</sup> Using Vegard's Law based on lattice parameter.<sup>d</sup> Using method described by Kim [61].

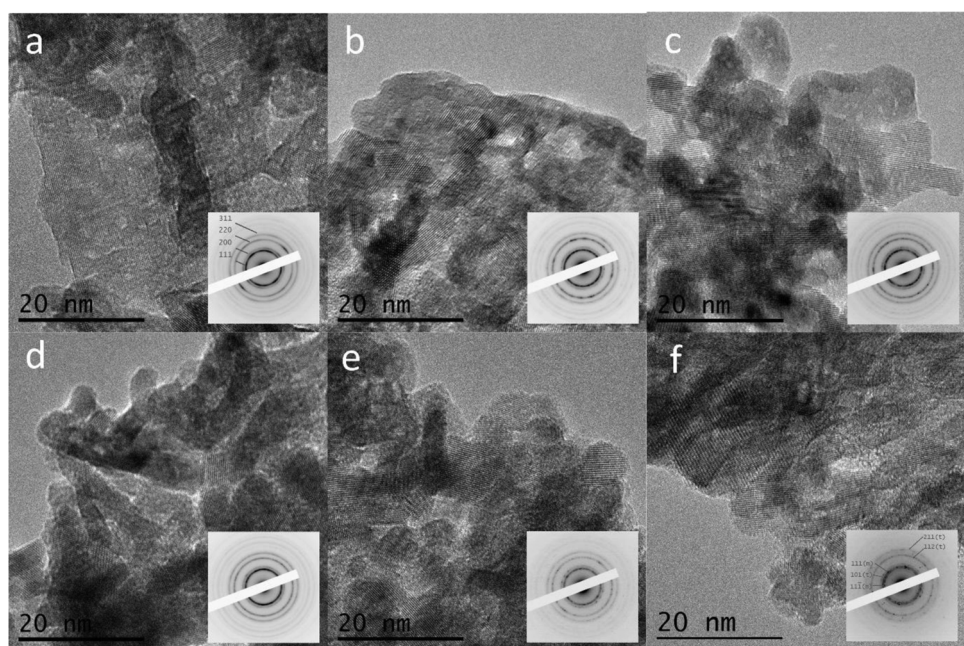


**Fig. 6.** High magnification TEM images of the  $\text{CeO}_2$ ,  $\text{ZrO}_2$  and  $\text{CeZrO}_x$  mixed metal oxide catalysts. Inset: selected area electron diffraction pattern of larger c.a. 250 nm areas. (a)  $\text{CeO}_2$ , (b)  $\text{Ce}_{0.95}\text{Zr}_{0.05}\text{O}_x$ , (c)  $\text{Ce}_{0.90}\text{Zr}_{0.10}\text{O}_x$ , (d)  $\text{Ce}_{0.75}\text{Zr}_{0.25}\text{O}_x$ , (e)  $\text{Ce}_{0.50}\text{Zr}_{0.50}\text{O}_x$  and (f)  $\text{ZrO}_2$ .

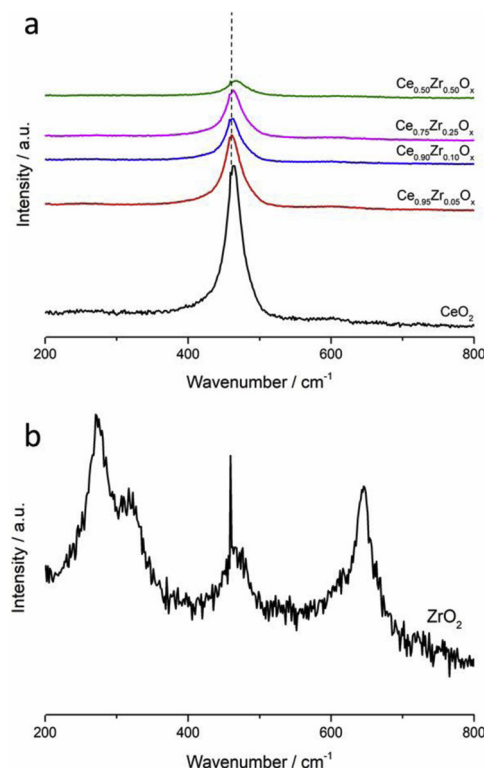


**Fig. 7.** Laser Raman spectra for the a.  $\text{CeO}_2$ ,  $\text{Ce}_{0.95}\text{Zr}_{0.05}\text{O}_x$ ,  $\text{Ce}_{0.90}\text{Zr}_{0.10}\text{O}_x$ ,  $\text{Ce}_{0.75}\text{Zr}_{0.25}\text{O}_x$  and  $\text{Ce}_{0.50}\text{Zr}_{0.50}\text{O}_x$  and b.  $\text{ZrO}_2$  (spectra enhanced by 7.5x) calcined at 400 °C. Laser  $\lambda = 514 \text{ nm}$ .

464  $\text{cm}^{-1}$  (Table 1). The FWHM value for pure  $\text{CeO}_2$  is 28.6  $\text{cm}^{-1}$  and increases steadily upon increase in Zr loading, with the  $\text{Ce}_{0.50}\text{Zr}_{0.50}\text{O}_x$  catalyst having the highest value of 44.9  $\text{cm}^{-1}$ . The value of the Raman band FWHM is inversely related to crystallite size [49], and concentration of oxygen vacancies in the  $\text{CeO}_2$  lattice [50]. The crystallite size determined by XRD does slightly decrease upon addition of Zr into the  $\text{CeO}_2$ , but remains in the range 95–105 Å for all ratios. However, as

the relationship between crystallite size and FWHM is not linear, other factors have to be considered for the increase of FWHM. Therefore, increasing FWHM values of the  $\text{CeZrO}_x$  mixed metal oxide catalysts can be attributed to the presence of oxygen vacancies on the surface of the mixed metal oxide catalysts. The increase in oxygen vacancies of the  $\text{CeZrO}_x$  mixed metal oxide catalysts compared to the  $\text{CeO}_2$  can lead to increased VOC total oxidation activity, as observed for toluene total oxidation [51].

Temperature programmed reduction profiles are shown in Fig. 8. The samples were pre-treated under a flow of He at 120 °C for 1 h prior to analysis. Reduction profiles were obtained by analysing ca. 30 mg of catalyst under a flow of 10%  $\text{H}_2$  in Ar (30 mL min<sup>-1</sup>) over a temperature range from ambient to 1100 °C with a ramp rate of 15 °C min<sup>-1</sup>.

Characteristic reduction of bulk phase  $\text{CeO}_2$  occurs around 800 °C, with surface reduction occurring around 500 °C, forming  $\text{CeO}_{2-x}$ . From the reduction profiles in Fig. 8, the  $\text{CeO}_2$  surface reduced at 515 °C and bulk phase reduction occurred at 822 °C. The  $\text{ZrO}_2$  reduction profile was different, with reduction in two regions, 450 °C and 530 °C, which can be assigned to reduction of the surface, and formation of bridging OH groups [52].

When Zr was incorporated into the  $\text{CeO}_2$  lattice, there was a change

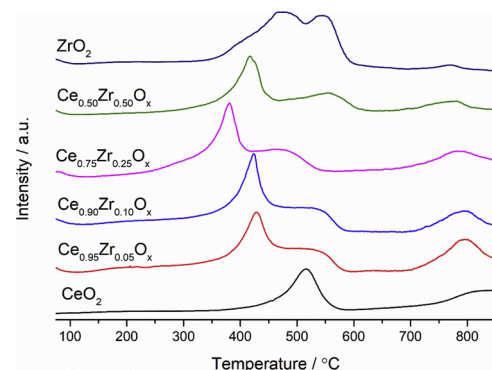


**Fig. 8.** Temperature-programmed reduction profiles of the  $\text{CeO}_2$ ,  $\text{ZrO}_2$  and  $\text{CeZrO}_x$  mixed metal oxide catalysts. Conditions: 30 mg sample under a 30 mL min<sup>-1</sup> 10%  $\text{H}_2$ /Ar flow over a temperature range 50–900 °C.

in the shape of the reduction profile compared to pure  $\text{CeO}_2$ . For the mixed ceria-zirconia two peaks were observed in the surface region and the temperature at which surface reduction occurred was significantly decreased compared to ceria. The temperature at which the bulk reduced also shifted to lower temperatures and the peak area decreased as Zr content of the  $\text{CeZrO}_x$  mixed metal oxides increased. The shift to lower temperatures for reduction of both surface and bulk  $\text{CeO}_2$  indicates the Zr enhances reducibility of the  $\text{CeO}_2$ , as noted by many studies [17–19,48]. The presence of two surface reduction peaks in the  $\text{CeZrO}_x$  mixed metal oxide catalysts suggests there is increased presence of  $\text{Ce}^{3+}$  compared to  $\text{CeO}_2$ , and accordingly implies an increase of surface oxygen vacancy defects.

A summary of  $\text{H}_2$  consumption for the surface of  $\text{CeZrO}_x$  mixed metal oxide catalysts is shown in Table 1.  $\text{CeO}_2$  had the lowest mass and surface area normalised  $\text{H}_2$  consumption, and consequently extent of reduction, compared to all of the  $\text{CeZrO}_x$  mixed metal oxide catalysts. When any amount of Zr was added into the  $\text{CeO}_2$  a significant increase in the extent of surface reduction was observed. The same effect was demonstrated previously with ceria-zirconia catalysts prepared using other methods, such as coprecipitation with urea [20]. The most active  $\text{CeZrO}_x$  mixed metal oxide catalyst,  $\text{Ce}_{0.90}\text{Zr}_{0.10}\text{O}_x$ , had the highest mass normalised surface  $\text{H}_2$  consumption, and the least active mixed metal oxide catalyst had the lowest. These data strongly suggest the extent of surface reduction is an influencing factor for catalyst activity, but it is not the only factor as surface area normalised reduction did not correlate directly with the order of catalyst activity, and hence other characteristics of the catalyst also exert an influence.

Secondary and backscattered electron images of both the  $\text{CeO}_2$  and the  $\text{ZrO}_2$  (Supplementary Material Figure S1) show that the pure ceria has a distinct morphology with a folded surface, as compared to the more typical fused crystallites of the  $\text{ZrO}_2$ . The Ceria morphology changes upon Zr addition (Supplementary Material Figure S2). There is no further change to the morphology with increasing Zr concentration. Furthermore, no phase separation can be seen on the micron scale as the backscattered signal shows uniform contrast (Supplementary Material Figure S2).

EDX elemental mapping is shown in Figure S3 (Supplementary Material). There is a homogeneous distribution of Ce and Zr on the nanometer scale for  $\text{CeZrO}_x$  mixed metal oxide catalysts, except the  $\text{Ce}_{0.50}\text{Zr}_{0.50}\text{O}_x$  catalyst. The  $\text{Ce}_{0.50}\text{Zr}_{0.50}\text{O}_x$  sample had large regions of Zr along with islands of Ce material. Bulk elemental analysis by EDX of the ceria only catalyst (Table 1) shows that no Zr was present, indicating negligible bulk incorporation from ball milling contamination. EDX analysis of the  $\text{CeZrO}_x$  mixed metal oxide catalysts demonstrates that the Ce and Zr contents were close to those expected from the synthesis ratios from the starting materials for all of the  $\text{CeZrO}_x$  mixed metal oxides. With the resulting bulk Ce:Zr ratios similar to the original synthesis values, there is a clear deviation between the Ce:Zr ratios incorporated into the lattice (Table 2) and the bulk Ce:Zr ratios (Table 1). Zirconium not incorporated into the  $\text{CeO}_2$  lattice may have formed amorphous  $\text{ZrO}_2$  on the surface of the ceria-zirconia, as previously reported for other  $\text{CeZrO}_x$  mixed metal oxides prepared using a related mechanochemical procedure [41].

The surface composition of the catalysts was examined by XPS, and quantitative surface concentrations are presented in Table 3. No Zr was observed on the pure  $\text{CeO}_2$  catalyst indicating no surface contamination occurred during the ball milling preparation, and is consistent with EDX bulk analysis. For the mixed oxides, despite EDX analysis revealing metal content close to that theoretically expected for the bulk materials at low concentrations of Zr, we note that from the XPS analysis the surface ratios deviate from the bulk ratios, and indicate surface enrichments of Zr. XRD analysis identified that not all of the zirconium added was incorporated into the cubic fluorite ceria lattice and the XPS confirms the additional Zr is distributed over the surface of the mixed oxide. A general trend is observed with the  $\text{CeZrO}_x$  mixed metal oxide catalysts, as lower surface concentrations of Zr produced catalysts that

were more active for propane and naphthalene total oxidation.

The relative concentration of near surface  $\text{Ce}^{3+}$  and  $\text{Ce}^{4+}$  was calculated by peak fitting the Ce 3d spectra [53] utilising models derived from pure  $\text{Ce}^{3+}$  and  $\text{Ce}^{4+}$  compounds (Fig. 9). There was no shift in the binding energy of Ce upon addition of any amount of Zr, however, the intensity of the Ce 3d signals of the  $\text{CeZrO}_x$  mixed metal oxide catalysts decrease compared to the  $\text{CeO}_2$  upon increasing Zr concentrations in the lattice. The majority of surface Ce was present in the  $\text{Ce}^{4+}$  oxidation state, with pure  $\text{CeO}_2$  prepared by the mechanochemical method exhibiting ca. 13%  $\text{Ce}^{3+}$ . As the Zr concentration increased, the near surface  $\text{Ce}^{3+}$  concentration in the  $\text{CeZrO}_x$  samples increased to the range ca. 20–35%. This is expected, and has been observed for many studies of ceria-zirconia, with the addition of Zr leading to an increase in the reducibility of the  $\text{CeO}_2$  lattice. This is also indicated by the extra surface reduction peak in TPR and change in Raman peak FWHM. All  $\text{CeZrO}_x$  mixed metal oxides exhibited increased surface  $\text{Ce}^{3+}$  concentration compared to the pure  $\text{CeO}_2$ . This increased surface  $\text{Ce}^{3+}$  content helps explain the enhancing effect of Zr addition to ceria, but does not correlate directly with activity, as the most active catalysts do not have the highest  $\text{Ce}^{3+}$  surface concentrations.

Fig. 10 shows the O 1s XPS spectra of the  $\text{CeZrO}_x$  mixed metal oxide catalysts. Two oxygen species are present on the surface of the  $\text{CeZrO}_x$  mixed metal oxide catalysts [54]. The region with a binding energy between 529–350 eV, denoted as  $\text{O}_\alpha$ , which is characteristic of lattice oxygen, and between 531–533 eV ( $\text{O}_\beta$ ), which are typically assigned to defective oxygen sites [54]. These defect oxygen species are reported to increase the activity of VOC total oxidation of  $\text{CeO}_2$  catalysts [55]. The relative amounts of both species are summarised in Table 3,  $\text{CeO}_2$  has 39.9% of  $\text{O}_\beta$  present on the surface. Both catalysts with low Zr content,  $\text{Ce}_{0.95}\text{Zr}_{0.05}\text{O}_x$  and  $\text{Ce}_{0.90}\text{Zr}_{0.10}\text{O}_x$ , had  $\text{O}_\beta$  greater than 50%, with the higher Zr loadings,  $\text{Ce}_{0.75}\text{Zr}_{0.25}\text{O}_x$  and  $\text{Ce}_{0.50}\text{Zr}_{0.50}\text{O}_x$ , having a surface  $\text{O}_\beta$  greater than 41%.

It is reported that the relative concentration of  $\text{O}_\beta$  correlates with naphthalene total oxidation activity for  $\text{CeO}_2$  catalysts doped with Cu [56]. For both propane [57] and naphthalene [58] total oxidation occurred via the Mars-van Krevelen mechanism, and hence the extent to which oxygen can be removed from the mixed metal oxide lattice is vital. This is controlled by the surface oxygen species, vacancies and other defects on the surface of the mixed metal oxide lattice, and to an extent the concentration of  $\text{Ce}^{3+}$  [59]. The effect of relative surface  $\text{O}_\beta$  concentration on the rate of propane total oxidation activity is shown in Fig. 11. The relative concentration of surface  $\text{O}_\beta$  has a significant correlation with propane total oxidation activity. The activity for propane total oxidation increases as the concentration of surface oxygen defects increase on the ceria-zirconia catalysts. The  $\text{Ce}_{0.50}\text{Zr}_{0.50}\text{O}_x$  has activity lower than may be expected from the correlation, but this catalyst has the highest concentration of zirconia remaining on the catalyst that is not incorporated into the  $\text{CeO}_2$  lattice, and this less active zirconia phase may block access to active sites. Indeed the presence of an amorphous zirconia component or non-dissolved  $\text{ZrO}_2$  sub units at the grain boundaries has been reported previously [32,41] and is evidenced here by the presence of very weak broad peaks in the XRD at 30.5° and 50.6° (Fig. 5). A broadly similar trend between surface  $\text{O}_\beta$  and naphthalene oxidation activity is also apparent, although the correlation is not as strong as for propane. Catalysts with lower concentrations of  $\text{O}_\beta$  ( $\text{Ce}_{0.75}\text{Zr}_{0.25}\text{O}_x$ ,  $\text{Ce}_{0.50}\text{Zr}_{0.50}\text{O}_x$  and  $\text{CeO}_2$ ), had lower activity compared to the catalysts  $\text{Ce}_{0.95}\text{Zr}_{0.05}\text{O}_x$  and  $\text{Ce}_{0.90}\text{Zr}_{0.10}\text{O}_x$  with higher relative surface concentrations of  $\text{O}_\beta$ .

#### 4. Conclusions

Mechanochemical preparation from nitrate precursors is a viable method to synthesise active  $\text{CeZrO}_x$  mixed metal oxide catalysts for the total oxidation of propane and naphthalene. The synthesis method led to catalysts containing solid solutions of  $\text{CeZrO}_x$  mixed metal oxide identified by XRD, laser Raman and electron microscopy. The

**Table 3**

X-ray Photoelectron Spectroscopy derived surface elemental concentrations (at%) for the series of  $\text{CeO}_2$ ,  $\text{ZrO}_2$  and  $\text{CeZrO}_x$  mixed metal oxide catalysts. Note for clarity, adventitious carbon is omitted from the table.

Catalyst	Concentration / at%				Relative Ce / %	Relative Zr / %	Relative $\text{O}_\alpha$ / %	Relative $\text{O}_\beta$ / %	$\text{Ce}^{3+}$ : $\text{Ce}^{4+}$ Ratio
	$\text{Ce}^{4+}$	$\text{Ce}^{3+}$	O 1 s	Zr 3d					
$\text{CeO}_2$	18.4	2.9	54.2	0	100	—	60.1	39.9	0.16
$\text{Ce}_{0.5}\text{Zr}_{0.5}\text{O}_x$	17.8	3.4	58.6	5.33	80.0	20.0	48.4	51.6	0.35
$\text{Ce}_{0.9}\text{Zr}_{0.1}\text{O}_x$	10.8	3.7	51.4	4.6	75.9	24.1	48.2	51.8	0.20
$\text{Ce}_{0.75}\text{Zr}_{0.25}\text{O}_x$	9.7	2.4	54.2	11.6	51.1	48.9	55.5	44.5	0.24
$\text{Ce}_{0.5}\text{Zr}_{0.5}\text{O}_x$	5.6	1.7	51.9	15.9	32.3	67.7	58.4	41.6	0.31
$\text{ZrO}_2$	0	0	57.1	27.6	—	100	—	—	n/a

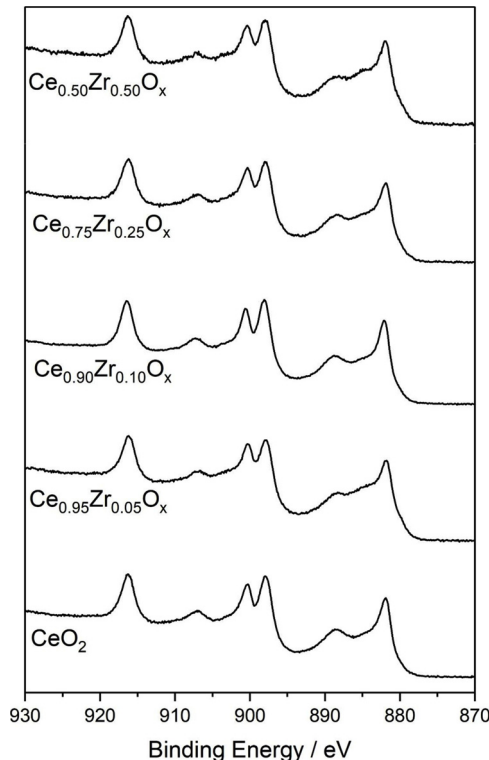


Fig. 9. XPS Spectra of the Ce 3d peaks for the calcined  $\text{CeO}_2$ ,  $\text{ZrO}_2$  and  $\text{CeZrO}_x$  mixed metal oxide catalysts.

incorporation of zirconium into the  $\text{CeO}_2$  cubic fluorite lattice increased the surface area compared to the pure  $\text{CeO}_2$  and  $\text{ZrO}_2$ , and there was an enrichment of Zr on the surface when concentrations were compared to the bulk. Incorporation of Zr also increased the surface ratio of  $\text{Ce}^{3+}$ : $\text{Ce}^{4+}$  in the  $\text{CeZrO}_x$  mixed metal oxide catalysts and enhanced catalyst surface reducibility. Low loadings of Zr produced the most active catalysts, with the  $\text{Ce}_{0.90}\text{Zr}_{0.10}\text{O}_x$  being the most active catalyst for total oxidation of propane and naphthalene. For propane a strong correlation between activity and surface oxygen defects was established, and although not as strong a similar correlation was apparent for naphthalene total oxidation.

#### Acknowledgements

The authors would like to acknowledge funding from Cardiff University, and experimental assistance from the Cardiff University Transmission Electron Microscopy Facility

#### Appendix A. Supplementary data

Supplementary material related to this article can be found, in the

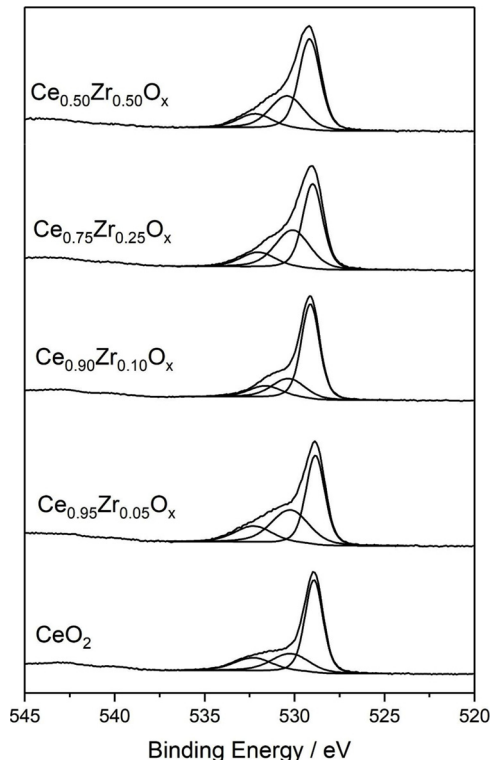


Fig. 10. XPS Spectra of the O 1 s peaks of the calcined  $\text{CeO}_2$ ,  $\text{ZrO}_2$  and  $\text{CeZrO}_x$  mixed metal oxide catalysts.

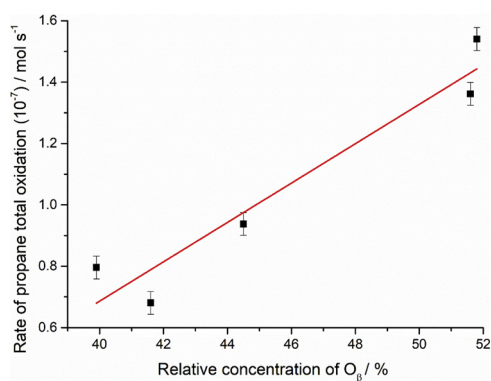


Fig. 11. Relationship between relative concentration of  $\text{O}_\beta$  measured from XPS and absolute rate of propane total oxidation at 450 °C.

online version, at doi:<https://doi.org/10.1016/j.apcatb.2019.04.061>.

## References

- [1] T.V. Choudhary, S. Banerjee, V.R. Choudhary, Catalysts for combustion of methane and lower alkanes, *Appl. Catal. A Gen.* 234 (2002) 1–23, [https://doi.org/10.1016/S0926-860X\(02\)00231-4](https://doi.org/10.1016/S0926-860X(02)00231-4).
- [2] J. Duan, J. Tan, L. Yang, S. Wu, J. Hao, Concentration, sources and ozone formation potential of volatile organic compounds (VOCs) during ozone episode in Beijing, *Atmos. Res.* 88 (2008) 25–35, <https://doi.org/10.1016/j.atmosres.2007.09.004>.
- [3] T.B. Ryerson, M. Trainer, J.S. Holloway, D.D. Parrish, L.G. Huey, D.T. Sueper, G.J. Frost, S.G. Donnelly, S. Schauffler, E.L. Atlas, W.C. Kuster, P.D. Goldan, G. Hubler, J.F. Meagher, F.C. Fehsenfeld, Observations of ozone formation in power plant plumes and implications for ozone control strategies, *Science* (80–) 292 (2001) 719–723, <https://doi.org/10.1126/science.1058113>.
- [4] F. Parungo, C. Nagamoto, R. Madel, A study of the mechanisms of acid rain formation, *J. Atmos. Sci.* 44 (1987) 3162–3174.
- [5] B.R. Gurjar, A. Jain, A. Sharma, A. Agarwal, P. Gupta, A.S. Nagpure, J. Lelieveld, Human health risks in megacities due to air pollution, *Atmos. Environ.* 44 (2010) 4606–4613, <https://doi.org/10.1016/j.atmosenv.2010.08.011>.
- [6] R.C. Flagan, J.H. Seinfeld, *Fundamentals of Air Pollution Engineering*, 1st ed., Prentice-Hall Inc., 1988.
- [7] [http://www.theglobaleconomy.com/rankings/lpg\\_consumption/](http://www.theglobaleconomy.com/rankings/lpg_consumption/), (n.d.).
- [8] V.R. Choudhary, G.M. Deshmukh, D.P. Mishra, Kinetics of the complete combustion of dilute propane and toluene over iron-doped ZrO<sub>2</sub> catalyst, *Energy Fuels* 19 (2005) 54–63, <https://doi.org/10.1021/ef0498871>.
- [9] A.S. Ramadas, *Alternative Fuels for Transportation*, 6th ed., CRC Press, 2011.
- [10] U.S. Environmental Protection Agency, Contaminant Candidate List Regulatory Determination Support Document for Naphthalene, (2003), p. 6.
- [11] C.S. Heneghan, G.J. Hutchings, S.H. Taylor, *Catalysis Volume 17*, The Royal Society of Chemistry, 2004.
- [12] R.K. Sharma, B. Zhou, S. Tong, K.T. Chuane, A. Tg, Catalytic destruction of volatile organic compounds using supported platinum and palladium hydrophobic catalysts, *Ind. Eng. Chem. Res.* (1995) 4310–4317.
- [13] F. Menegazzo, P. Burti, M. Signoretto, M. Manzoli, S. Vankova, F. Bocuzzi, F. Pinna, G. Strukul, Effect of the addition of Au in zirconia and ceria supported Pd catalysts for the direct synthesis of hydrogen peroxide, *J. Catal.* 257 (2008) 369–381, <https://doi.org/10.1016/j.jcat.2008.05.019>.
- [14] V. Shapovalov, H. Metiu, Catalysis by doped oxides: CO oxidation by Au<sub>x</sub>Ce<sub>1-x</sub>O<sub>2</sub>, *J. Catal.* 245 (2007) 205–214, <https://doi.org/10.1016/j.jcat.2006.10.009>.
- [15] X.S. Huang, H. Sun, L.C. Wang, Y.M. Liu, K.N. Fan, Y. Cao, Morphology effects of nanoscale ceria on the activity of Au/CeO<sub>2</sub> catalysts for low-temperature CO oxidation, *Appl. Catal. B Environ.* 90 (2009) 224–232, <https://doi.org/10.1016/j.apcatb.2009.03.015>.
- [16] X. Zhang, H. Shi, B.Q. Xu, Comparative study of Au/ZrO<sub>2</sub> catalysts in CO oxidation and 1,3-butadiene hydrogenation, *Catal. Today* 122 (2007) 330–337, <https://doi.org/10.1016/j.cattod.2007.02.016>.
- [17] M. Thammachart, V. Meeyoo, T. Risksomboon, S. Osuwan, Catalytic activity of CeO<sub>2</sub> – ZrO<sub>2</sub> mixed oxide catalysts prepared via sol – gel technique: CO oxidation, *Catal. Today* 68 (2001) 53–61, [https://doi.org/10.1016/S0920-5861\(01\)00322-4](https://doi.org/10.1016/S0920-5861(01)00322-4).
- [18] S. Bedrane, C. Descorme, D. Duprez, Investigation of the oxygen storage process on ceria- and ceria-zirconia-supported catalysts, *Catal. Today* 75 (2002) 401–405, [https://doi.org/10.1016/S0920-5861\(02\)00089-5](https://doi.org/10.1016/S0920-5861(02)00089-5).
- [19] M. Boaro, The dynamics of oxygen storage in ceria-zirconia model catalysts measured by CO oxidation under stationary and cycling feedstream compositions, *J. Catal.* 193 (2000) 338–347, <https://doi.org/10.1006/jcat.2000.2887>.
- [20] D.R. Sellick, A. Aranda, T. García, J.M. López, B. Solsona, A.M. Mastral, D.J. Morgan, A.F. Carley, S.H. Taylor, Influence of the preparation method on the activity of ceria zirconia mixed oxides for naphthalene total oxidation, *Appl. Catal. B Environ.* 132–133 (2013) 98–106, <https://doi.org/10.1016/j.apcatb.2012.11.036>.
- [21] A. Bampenrat, V. Meeyoo, B. Kitiyanan, P. Rangsuvigit, T. Rirkosomboon, Catalytic oxidation of naphthalene over CeO<sub>2</sub>–ZrO<sub>2</sub> mixed oxide catalysts, *Catal. Commun.* 9 (2008) 2349–2352, <https://doi.org/10.1016/j.catcom.2008.05.029>.
- [22] F. Zamar, A. Trovarelli, C. de Leitenburg, G. Dolcetti, CeO<sub>2</sub>-based solid solutions with the fluorite structure as novel and effective catalysts for methane combustion, *J. Chem. Soc. Chem. Commun.* 02 (1995) 965, <https://doi.org/10.1039/c39950000965>.
- [23] H. Omidvarbona, A. Kumar, D.S. Kim, Recent studies on soot modeling for diesel combustion, *Renew. Sustain. Energy Rev.* 48 (2015) 635–647, <https://doi.org/10.1016/j.rser.2015.04.019>.
- [24] B. Wang, X. Wu, R. Ran, Z. Si, D. Weng, IR characterization of propane oxidation on Pt/CeO<sub>2</sub>–ZrO<sub>2</sub>: The reaction mechanism and the role of Pt, *J. Mol. Catal. A Chem.* 356 (2012) 100–105, <https://doi.org/10.1016/j.molcata.2011.12.030>.
- [25] B. Wang, X. Wu, R. Ran, Z. Si, D. Weng, Participation of sulfates in propane oxidation on Pt/SO<sub>4</sub><sup>2-</sup>/CeO<sub>2</sub>–ZrO<sub>2</sub> catalyst, *J. Mol. Catal. A Chem.* 361–362 (2012) 98–103, <https://doi.org/10.1016/j.molcata.2012.05.007>.
- [26] P.T. Anastas, J.C. Warner, *Green Chemistry Theory and Practice*, Oxford University Press, New York, 1998.
- [27] K. Ralphs, C. Hardacre, S.L. James, Application of heterogeneous catalysts prepared by mechanochemical synthesis, *Chem. Soc. Rev.* 42 (2013) 7701–7718, <https://doi.org/10.1039/c3cs60066a>.
- [28] A.A. Mirzaei, H.R. Shaterian, R.W. Joyner, M. Stockenhuber, S.H. Taylor, G.J. Hutchings, Ambient temperature carbon monoxide oxidation using copper manganese oxide catalysts: effect of residual Na<sup>+</sup> acting as catalyst poison, *Catal. Commun.* 4 (2003) 17–20, [https://doi.org/10.1016/S1566-7367\(02\)00231-5](https://doi.org/10.1016/S1566-7367(02)00231-5).
- [29] Q. Dong, S. Yin, C. Guo, T. Sato, A new oxygen storage capacity material of a tin-doped ceria-zirconia-supported palladium-alumina catalyst with high CO oxidation activity, *Chem. Lett.* 41 (2012) 1250–1252, <https://doi.org/10.1246/cl.2012.1250>.
- [30] G. Hutchings, R. Higgins, Selective oxidation of n-butane to maleic anhydride with vanadium phosphorus catalysts prepared by communition in the presence of dispersants, *Appl. Catal. A Gen.* 154 (1997) 103–115, [https://doi.org/10.1016/S0926-860X\(96\)00368-7](https://doi.org/10.1016/S0926-860X(96)00368-7).
- [31] A. Suda, T. Kandori, N. Terao, Y. Ukyo, H. Sobukawa, M. Suguri, Formation of CeO<sub>2</sub>–ZrO<sub>2</sub> solid solution during attrition milling of CeO<sub>2</sub> powder, *J. Mater. Sci. Lett.* 17 (1997) 89–90, <https://doi.org/10.1023/A:1006514329090>.
- [32] Y.L. Chen, M. Qi, D.Z. Yang, K.H. Wu, Mechanical alloying of ceramics in zirconia-ceria system, *Mater. Sci. Eng. A* 183 (1994) L9–L12, [https://doi.org/10.1016/0921-5093\(94\)90915-6](https://doi.org/10.1016/0921-5093(94)90915-6).
- [33] A. Trovarelli, G. Dolcetti, J. Llorca, J.T. Kiss, F. Zamar, C. de Leitenburg, Nanophase fluorite-structured CeO<sub>2</sub>–ZrO<sub>2</sub> Catalysts prepared by high-energy mechanical milling, *J. Catal.* 169 (2002) 490–502, <https://doi.org/10.1006/jcat.1997.1705>.
- [34] C.A. Strydom, C.P.J. van Vuuren, The thermal decomposition of cerium(III) nitrate, *J. Therm. Anal.* 32 (1987) 157–160, <https://doi.org/10.1007/BF01914558>.
- [35] F. Zhang, C.-H. Chen, J.C. Hanson, R.D. Robinson, I.P. Herman, S.-W. Chan, Phases in ceria-zirconia binary oxide (1-x)CeO<sub>2</sub>-xZrO<sub>2</sub> nanoparticles: the effect of particle size, *J. Am. Ceram. Soc.* 89 (2006) 1028–1036, <https://doi.org/10.1111/j.1551-2916.2005.00788.x>.
- [36] R. Grau-Crespo, N.H. de Leeuw, S. Hamad, U.V. Waghmare, Phase separation and surface segregation in ceria-zirconia solid solutions, *Proc. R. Soc. A Math. Phys. Eng. Sci.* 467 (2011) 1925–1938, <https://doi.org/10.1088/rspa.2010.0512>.
- [37] R. Di Monte, J. Kašpar, Nanostructured CeO<sub>2</sub>–ZrO<sub>2</sub> mixed oxides, *J. Mater. Chem.* 15 (2005) 633–648, <https://doi.org/10.1039/B414244F>.
- [38] C. Bozo, F. Gaillard, N. Guilhaume, Characterisation of ceria-zirconia solid solutions after hydrothermal ageing, *Appl. Catal. A Gen.* 220 (2001) 69–77, [https://doi.org/10.1016/S0926-860X\(01\)00710-4](https://doi.org/10.1016/S0926-860X(01)00710-4).
- [39] C. Bozo, N. Guilhaume, E. Garbowski, M. Primet, Combustion of methane on CeO<sub>2</sub>–ZrO<sub>2</sub> based catalysts, *Catal. Today* 59 (2000) 33–45, [https://doi.org/10.1016/S0920-5861\(00\)00270-4](https://doi.org/10.1016/S0920-5861(00)00270-4).
- [40] A. Hirano, A. Suda, Oxygen storage capacity, specific surface area, and pore-size distribution of ceria-zirconia solid solutions directly formed by thermal hydrolysis, *J. Am. Ceram. Soc.* 86 (2003) 2209–2211.
- [41] I.A. Carbalj-Ramos, J. Andrade-Gamboa, F.C. Gennari, Nanostructured Ce<sub>1-x</sub>Zr<sub>x</sub>O<sub>2</sub> solid solutions produced by mechanochemical processing, *Mater. Chem. Phys.* 137 (2013) 1073–1080, <https://doi.org/10.1016/j.matchemphys.2012.11.039>.
- [42] T. Garcia, B. Solsona, S.H. Taylor, Nano-crystalline Ceria catalysts for the abatement of polycyclic aromatic hydrocarbons, *Catal. Letters* 105 (2005) 183–189, <https://doi.org/10.1007/s10562-005-8689-2>.
- [43] M. Teng, L. Luo, X. Yang, Synthesis of mesoporous Ce<sub>1-x</sub>Zr<sub>x</sub>O<sub>2</sub> (x = 0.2–0.5) and catalytic properties of CuO based catalysts, *Microporous Mesoporous Mater.* 119 (2009) 158–164, <https://doi.org/10.1016/j.micromeso.2008.10.019>.
- [44] L. Chen, T. Mashimo, E. Omurzak, H. Okudera, C. Iwamoto, A. Yoshiasa, Pure tetragonal ZrO<sub>2</sub> nanoparticles synthesized by pulsed plasma in liquid, *J. Phys. Chem. C* 115 (2011) 9370–9375, <https://doi.org/10.1021/jp111367k>.
- [45] S. Deshpande, S. Patil, S.V. Kuchibhatla, S. Seal, Size dependency variation in lattice parameter and valency states in nanocrystalline cerium oxide, *Appl. Phys. Lett.* 87 (2005) 1–3, <https://doi.org/10.1063/1.2061873>.
- [46] S. Damyanova, B. Pawelec, K. Arishtiava, M.V.M. Huerta, J.L.G. Fierro, Study of the surface and redox properties of ceria-zirconia oxides, *Appl. Catal. A Gen.* 337 (2008) 86–96, <https://doi.org/10.1016/j.apcata.2007.12.005>.
- [47] L. Vegard, The constitution of the mixed crystals and the filling of the atoms, *J. Phys. 5* (1921) 17–26.
- [48] G. Vlaic, R. Di Monte, P. Fornasiero, E. Fonda, J. Kašpar, M. Graziani, Redox property-local structure relationships in the Rh-loaded CeO<sub>2</sub>–ZrO<sub>2</sub> mixed oxides, *J. Catal.* 182 (1999) 378–389, <https://doi.org/10.1006/jcat.1998.2335>.
- [49] J.E. Spanier, R.D. Robinson, F. Zhang, S.-W. Chan, I.P. Herman, Size-dependent properties of CeO<sub>2</sub>-y nanoparticles as studied by Raman scattering, *Phys. Rev. B* 64 (2001) 245407, , <https://doi.org/10.1103/PhysRevB.64.245407>.
- [50] I. Kosacki, T. Suzuki, H.U. Anderson, P. Colombari, Raman scattering and lattice defects in nanocrystalline CeO<sub>2</sub> thin films, *Solid State Ion.* 149 (2002) 99–105, [https://doi.org/10.1016/S0167-2738\(02\)00104-2](https://doi.org/10.1016/S0167-2738(02)00104-2).
- [51] J.M. López, A.L. Gilbank, T. García, B. Solsona, S. Agouram, L. Torrente-Murciano, The prevalence of surface oxygen vacancies over the mobility of bulk oxygen in nanostructured ceria for the total toluene oxidation, *Appl. Catal. B Environ.* 174–175 (2015) 403–412, <https://doi.org/10.1016/j.apcatb.2015.03.017>.
- [52] J.M. Pigos, C.J. Brooks, G. Jacobs, B.H. Davis, Low temperature water-gas shift: characterization of Pt-based ZrO<sub>2</sub> catalyst promoted with Na discovered by combinatorial methods, *Appl. Catal. A Gen.* 319 (2007) 47–57, <https://doi.org/10.1016/j.apcata.2006.11.014>.
- [53] F. Zhang, P. Wang, J. Koberstein, S. Khalid, S.W. Chan, Cerium oxidation state in ceria nanoparticles studied with X-ray photoelectron spectroscopy and absorption near edge spectroscopy, *Surf. Sci.* 563 (2004) 74–82, <https://doi.org/10.1016/j.susc.2004.05.138>.
- [54] A. Galtayries, R. Sporken, J. Riga, G. Blanchard, R. Caudano, XPS comparative study of ceria/zirconia mixed oxides: powders and thin film characterisation, *J. Electron. Spectros. Relat. Phenomena.* 88–91 (1998) 951–956, [https://doi.org/10.1016/S0368-2048\(97\)00134-5](https://doi.org/10.1016/S0368-2048(97)00134-5).
- [55] E.N. Ntaijua, T.E. Davies, T. Garcia, B. Solsona, S.H. Taylor, Influence of preparation conditions of nano-crystalline ceria catalysts on the total oxidation of naphthalene, a model polycyclic aromatic hydrocarbon, *Catal. Lett.* 141 (2011) 1732–1738, <https://doi.org/10.1007/s10562-011-0710-3>.

- [56] A. Aranda, E. Aylón, B. Solsona, R. Murillo, A.M. Mastral, D.R. Sellick, S. Agouram, T. García, S.H. Taylor, High activity mesoporous copper doped cerium oxide catalysts for the total oxidation of polycyclic aromatic hydrocarbon pollutants, *Chem. Commun. (Camb.)* 48 (2012) 4704–4706, <https://doi.org/10.1039/c2cc31206a>.
- [57] V. Balcaen, R. Roelant, H. Poelman, D. Poelman, G.B. Marin, TAP study on the active oxygen species in the total oxidation of propane over a CuO-CeO<sub>2</sub>/γ-Al<sub>2</sub>O<sub>3</sub>catalyst, *Catal. Today* 157 (2010) 49–54, <https://doi.org/10.1016/j.cattod.2010.02.048>.
- [58] E. Ntanjua N, S.H. Taylor, The catalytic total oxidation of polycyclic aromatic hydrocarbons, *Top. Catal.* 52 (2009) 528–541, <https://doi.org/10.1007/s11244-009-9180-x>.
- [59] A. Aranda, S. Agouram, J.M. López, A.M. Mastral, D.R. Sellick, B. Solsona, S.H. Taylor, T. García, Oxygen defects: the key parameter controlling the activity and selectivity of mesoporous copper-doped ceria for the total oxidation of naphthalene, *Appl. Catal. B Environ.* 127 (2012) 77–88, <https://doi.org/10.1016/j.apcatb.2012.07.033>.
- [60] G. Katz, X-ray diffraction powder pattern of metastable cubic ZrO<sub>2</sub>, *J. Am. Ceram. Soc.* 54 (1971) 531, <https://doi.org/10.1111/j.1151-2916.1971.tb12197.x>.
- [61] D.-J. Kim, Lattice parameters, ionic conductivities, and solubility limits in fluorite-structure MO<sub>2</sub> oxide [M = Hf<sup>4+</sup>, Zr<sup>4+</sup>, Ce<sup>4+</sup>, Th<sup>4+</sup>, U<sup>4+</sup>] solid solutions, *J. Am. Ceram. Soc.* 72 (1989) 1415–1421, <https://doi.org/10.1111/j.1151-2916.1989.tb07663.x>.